




Simultaneous multislice EPI prospective motion correction by real-time receiver phase correction and coil sensitivity map interpolation

Bo Li¹  | Ningzhi Li² | Ze Wang¹ | Radu Balan³  | Thomas Ernst¹ 

¹Department of Diagnostic Radiology and Nuclear Medicine, University of Maryland, Baltimore, Maryland USA

²U.S. Food Drug Administration, Silver Spring, Maryland USA

³Department of Mathematics, University of Maryland, College Park, Maryland USA

Correspondence

Thomas Ernst, Department of Diagnostic Radiology and Nuclear Medicine, University of Maryland, 670 W Baltimore St., HSF-III ROOM 1130A, Baltimore, MD 21201, USA.

Email: ternst@som.umaryland.edu

Funding information

National Institutes of Health, Grant/Award Numbers: 1UL1TR003098, P41EB029460-01A1, R01AG060054, R01AG070227, R01DA021146, R01EB031080-01A1, R21AG082435; National Science Foundation, Grant/Award Number: DMS-2108900; Simons Foundation, Grant/Award Number: 818333

Abstract

Purpose: To improve the image reconstruction for prospective motion correction (PMC) of simultaneous multislice (SMS) EPI of the brain, an update of receiver phase and resampling of coil sensitivities are proposed and evaluated.

Methods: A camera-based system was used to track head motion (3 translations and 3 rotations) and dynamically update the scan position and orientation. We derived the change in receiver phase associated with a shifted field of view (FOV) and applied it in real-time to each k-space line of the EPI readout trains. Second, for the SMS reconstruction, we adapted resampled coil sensitivity profiles reflecting the movement of slices. Single-shot gradient-echo SMS-EPI scans were performed in phantoms and human subjects for validation.

Results: Brain SMS-EPI scans in the presence of motion with PMC and no phase correction for scan plane shift showed noticeable artifacts. These artifacts were visually and quantitatively attenuated when corrections were enabled. Correcting misaligned coil sensitivity maps improved the temporal SNR (tSNR) of time series by 24% ($p = 0.0007$) for scans with large movements (up to ~ 35 mm and 30°). Correcting the receiver phase improved the tSNR of a scan with minimal head movement by 50% from 50 to 75 for a United Kingdom biobank protocol.

Conclusion: Reconstruction-induced motion artifacts in single-shot SMS-EPI scans acquired with PMC can be removed by dynamically adjusting the receiver phase of each line across EPI readout trains and updating coil sensitivity profiles during reconstruction. The method may be a valuable tool for SMS-EPI scans in the presence of subject motion.

KEYWORDS

coil sensitivity interpolation, motion artifacts, prospective motion correction, real-time phase correction, SMS-EPI

1 | INTRODUCTION

Single-shot 2D echo-planar imaging (EPI)¹ is widely used for functional MRI (fMRI) and diffusion weighted imaging (DWI).² The short scan time of EPI enables whole-brain coverage in seconds, which facilitates studies of the structure and function of the brain. However, fMRI requires multiple repetitions to obtain stable estimates of the small functional signals (typically a few percent).^{3–5} Consequently, even small head movements can induce substantial errors in functional signals.^{6–8}

Simultaneous multislice (SMS) techniques provide a major advance for EPI scans by acquiring multiple slices simultaneously and using RF coil profiles to reconstruct individual slices.^{9–11} Because SMS considerably reduces volume acquisition times, it is widely used in fMRI.^{5,9,11–13} However, typical SMS fMRI scan times continue to be long, because of the need to observe brain function over sufficient time periods. Hence, fMRI scans continue to be sensitive to subject movements, and EPI techniques that are robust to motion are desirable.

Methods for reducing motion-induced artifacts in MRI can be generally classified into retrospective¹⁴ and prospective motion correction (PMC) approaches.¹⁵ Retrospective techniques modify the MR k-space or image data during reconstruction,^{16–18} commonly in an iterative manner,¹⁴ but cannot guarantee sufficiently dense sampling of k-space during large rotations.¹⁹ Conversely, PMC methods keep the acquisition FOV aligned with the moving object, which maintains adequate and uniform sampling of k-space and can correct for larger movements.^{20,21} PMC techniques use MR-based navigators^{22–26} or external tracking devices, such as cameras,^{21,27–30} to track head movements and send tracking data to the scanner. The tracking data are used to update sequence parameters in real time (i.e., gradient orientation for rotations and RF frequency and phase for translations) to keep the FOV aligned with the moving object.

Fast optical tracking systems have been used to improve the quality of data in fMRI scans. For instance, PMC is beneficial for fMRI studies requiring accurate voxel registration across time, even when participants are instructed not to move during scans.²⁷ Likewise, an optical PMC system improved the stability of fMRI signals compared to acquisitions without PMC, and the sensitivity to detect brain activation was achieved without reducing specificity.³¹ In another fMRI study, PMC considerably reduced the rate of false positive activations at 7 T and increased statistical power.³²

However, despite the many advantages of PMC techniques, dynamically adjusting scan parameters in SMS acquisitions can introduce secondary effects that commonly are not corrected. In this study, we used a

camera-based tracking system for PMC of a gradient-echo SMS-EPI sequence and found that motion artifacts remained after image reconstruction. Two separate sources contributed to these artifacts. First, dynamic updates of slice translations induce phase changes across SMS-encoding steps, which in turn can cause ghost artifacts if uncorrected. Second, motion updates of the FOV result in unaccounted changes in calibration data for moving slice objects (relative to stationary RF coils) and ultimately lead to reconstruction artifacts. We eliminated these artifacts by adjusting the receiver phase in real time and updating coil sensitivity profiles during SMS reconstruction. Phantom and in vivo experiments were carried out to validate the proposed techniques.

2 | THEORY

2.1 | Real-time receiver phase update with prospective motion correction applied

The blipped-controlled aliasing in parallel imaging (blipped-CAIPI) sequence was developed to reduce the g-factor and improve the reconstruction quality of SMS imaging by introducing an in-plane image shift in acquisitions.³³ A train of blips in slice direction (G_z) is applied simultaneously with the phase encoding (PE) blips to create interslice image shifts in the PE direction for off-center slices. Within the echo train, the G_z blips induce a phase accumulation that depends on the location of each of the simultaneously excited slices. For two simultaneously excited slices, the phase accumulation θ at the phase encoding step N_y for the bottom slice at position z is

$$\theta(z, N_y) = \sum_{n_y=1}^{N_y} \gamma A_{\text{blip}}(n_y) z, \quad (1)$$

where γ is the gyromagnetic ratio, and $A_{\text{blip}}(n_y)$ is the G_z blip area for the phase encoding step n_y . A FOV/2 shift in image domain usually minimizes aliasing artifacts for the two-slices case. Therefore, we have $\gamma |A_{\text{blip}}| z_{\text{gap}} = \pi$ and $|A_{\text{blip}}| = \pi/\gamma z_{\text{gap}}$, where z_{gap} is the center-to-center distance of the two slices. When the blipped-CAIPI encoding scheme (i.e., $G_z, -G_z, G_z, \dots, -G_z$ with a prewinding lobe $-G_z/2$) is applied, the phase $\theta(z, N_y)$ of the bottom slice is $\pi z/2z_{\text{gap}}, -\pi z/2z_{\text{gap}}, \pi z/2z_{\text{gap}}, \dots, -\pi z/2z_{\text{gap}}$ (the prewinding lobe generates $-\pi z/2z_{\text{gap}}$ prephase for the bottom slice). Because the receiver phase of the twofold SMS sequence equals that of the bottom slice, the phase has to be set to $\theta(z, N_y)$ during acquisition to prevent an $N/2$ PE ghost during reconstruction. A similar analysis applies to cases with three and more simultaneous slices.

Let us assume that a PMC update from one SMS excitation to the next shifts slice positions by Δz . Starting with Eq. (1), the effect of this update on the phase is

$$\begin{aligned} \theta(z + \Delta z, N_y) &= \sum_{n_y=1}^{N_y} \gamma A_{\text{blip}}(n_y)(z + \Delta z) = \theta(z, N_y) \\ &+ \sum_{n_y=1}^{N_y} \gamma A_{\text{blip}}(n_y) \Delta z. \end{aligned} \quad (2)$$

Substituting δ for the second term in Eq. (2) yields

$$\delta(\Delta z, N_y) = \sum_{n_y=1}^{N_y} \gamma A_{\text{blip}}(n_y) \Delta z, \quad (3)$$

$$\theta(z + \Delta z, N_y) = \theta(z, N_y) + \delta(\Delta z, N_y). \quad (4)$$

Eq. (4) demonstrates that a PMC-induced translation Δz in slice direction causes an additional phase $\delta(\Delta z, N_y)$. For an SMS factor of 2, this additional phase leads to $N/2$ phase encoding ghosts during image reconstruction because it alternates from one phase encoding step (N_y) to the next. However, Eq. (3) demonstrates that the additional phase is not dependent on the absolute slice position. Therefore, it is possible to adjust the receiver phase in real-time for each echo (readout) in the EPI train by $\delta(\Delta z, N_y)$ to eliminate PE ghosts. The other five motion parameters (i.e., x, y translations and x, y, z rotations) do not contribute to δ .

2.2 | Motion-induced variations in spatial sensitivity encoding

The k-space signal m in readout direction (i.e., k-space line) for the PE step l and channel j is given by

$$m_{l,j} = \int \rho(\mathbf{r}) e^{-i\mathbf{k}_l \mathbf{r}} C_j(\mathbf{r}) d\mathbf{r}, \quad (5)$$

where ρ is spin density, \mathbf{r} denotes position, and C is the coil sensitivity. Here, we assume that motion is essentially frozen within each k-space line, which is reasonable because of the short duration of each individual readout (~ 0.5 ms). Therefore, the motion is considered discrete between k-space lines, and the receiver phase can be adjusted for each line according to the current slice translation. In the presence of motion, for a particular point at time t with PMC enabled, Eq. (5) becomes,

$$m_{l,j,t} = \int \rho(\mathbf{r}) e^{-i\mathbf{k}_l \mathbf{r}} C'_{j,t}(\mathbf{r}) d\mathbf{r}, \quad (6)$$

where \mathbf{k}_l is invariant because of the fixed k-space size and step, and \mathbf{r} is also invariant because the PMC continuously adjusts the FOV to follow the moving object. However, the PMC-induced change in the FOV introduces a mismatch in coil sensitivity encodings between the reference $C_j(\mathbf{r})$ and acquisition $C'_{j,t}(\mathbf{r})$ scans, which may cause artifacts during reconstruction.³⁴ Therefore, PMC updates require a change in the coil sensitivity maps (CSMs) used for SMS reconstructions, based on either SENSE using the multiple coil sensitivity equation¹⁰ or slice-GRAPPA.^{33,35}

2.3 | SMS reconstruction

2.3.1 | SENSE

The aliased pixels can be unfolded with SENSE reconstruction using a pixel-by-pixel inversion of the coil sensitivity matrix, which contains single-slice coil profiles calculated from a pre-scan. For N simultaneously excited slices (i.e., the SMS acceleration factor is N), the aliased signal intensity $I^j(x, y)$ of the pixel of coil j and location (x, y) is

$$I^j(x, y) = \sum_{n=1}^N C_n^j(x, y) m_n(x, y), \quad (7)$$

where C_n^j is the sensitivity profile of coil j for slice n , and m_n is the actual magnetization of slice n . The most general solution to Eq. (7) is the pseudoinverse³⁶:

$$\widehat{\mathbf{M}}(x, y) = [(\mathbf{C}^* \mathbf{C})^{-1} \mathbf{C}^*] \mathbf{I}, \quad (8)$$

where the operator $*$ refers to the complex conjugate transpose, and \mathbf{C} is the coil sensitivity matrix of all coils and slices. The aliased image matrix is $\mathbf{I} = [I_{(x,y)}^1, I_{(x,y)}^2, \dots, I_{(x,y)}^{N_c}]^T$, and the solution $\widehat{\mathbf{M}} = [\widehat{\mathbf{M}}_{1(x,y)}, \widehat{\mathbf{M}}_{2(x,y)}, \dots, \widehat{\mathbf{M}}_{N(x,y)}]^T$ is the reconstruction of N slices at the location (x, y) .

With PMC enabled, coil profiles as seen by the moving slices (mobile reference frame) can be calculated by applying the inverse motion to the physical (stationary) coil profiles. Therefore, the solution of Eq. (8) becomes

$$\widehat{\mathbf{M}}' = [(\mathbf{C}'^* \mathbf{C}')^{-1} \mathbf{C}'^*] \mathbf{I}', \quad (9)$$

where \mathbf{I}' is the acquired SMS aliased image with motion, and \mathbf{C}' is the coil sensitivity matrix in the new (mobile) reference frame. \mathbf{C}' is generally unknown but can be

estimated from the known coil sensitivity profiles of the prescan.

2.4 | Split slice-GRAPPA

The split slice-GRAPPA (SP-SG) method uses reference data for fitting kernels to reduce dependencies on image contrast and the associated signal leakage artifacts.³⁵ In SP-SG reconstruction, the weight coefficients create an entirely new set of k-space data for each coil of a given slice. The weight to synthesize the data of coil j at location $z \in [1, 2, \dots, N]$ is

$$\mathbf{w}_z^j = \left(\sum_{s=1}^N (\mathbf{k}_s^* \mathbf{k}_s) \right)^{-1} \mathbf{k}_z^* \mathcal{T}_z^j, \quad (10)$$

where N is the number of slices, and $\mathbf{k}_1 \cdots \mathbf{k}_s$ are convolution matrices across all channels determined from the prescan reference data. \mathcal{T}_z^j is the j th channel of reference data at slice location z .

In the presence of motion, ghost artifacts may appear if there is a mismatch in coil weights between the reference and acquisition scans. In this situation, SP-SG weights can be updated by replacing \mathbf{K} and \mathcal{T} with the updated convolution matrix \mathbf{K}' and single-slice data \mathcal{T}' at new position. Therefore, Eq. (10) becomes

$$\mathbf{w}_z^j = \left(\sum_{s=1}^N (\mathbf{k}_s'^* \mathbf{k}_s') \right)^{-1} \mathbf{k}_z'^* \mathcal{T}_z'^j. \quad (11)$$

Therefore, motion-induced SMS artifacts can then be eliminated by using the weight coefficients \mathbf{W}' . \mathcal{K}' and \mathcal{T}' can be obtained from the updated reference data, which equals the original reference data multiplied by updated CSMs. In this study, to decrease the g-factor, the SP-SG kernels fitting was implemented with the Tikhonov regularization.³⁷ Therefore, we can rewrite Eq. (11) as

$$\mathbf{w}_z^j = \left(\sum_{s=1}^N (\mathbf{k}_s'^* \mathbf{k}_s') + \lambda \bar{\mathbf{I}} \right)^{-1} \mathbf{k}_z'^* \mathcal{T}_z'^j, \quad (12)$$

where $\bar{\mathbf{I}}$ is the identity matrix, λ is the regularization parameter computed by

$$\lambda = \frac{1}{q} \left\| \mathbf{k}_z'^* \mathcal{T}_z'^j \right\|_2, \quad (13)$$

and q is the scalar equal to the number of elements in the kernel multiplied by the number of coil channels used for acquisition.

3 | METHODS

3.1 | Interpolation of CSMs

When the scanned object moves to a new location, revised CSMs associated with the new slice locations should be used for SMS reconstruction. These updated sensitivity maps can be estimated by interpolating (or extrapolating) the original CSMs from the reference scan because CSMs vary smoothly in space. The interpolation constructs updated CSMs that best estimate the “true” value of the underlying coil sensitivity function in the mobile reference frame from the discrete set of initial maps. The underlying functions are assumed to be continuous and smooth in both magnitude and phase. The initial CSMs for each channel and slice were calculated using the eigenvector-based parallel imaging (ESPIRiT; 2D version) technique,³⁸ which can generate robust high-quality sensitivity maps by an eigenvalue decomposition of a calibration matrix in image space. Maps with the largest eigenvalues were used as CSMs.

Magnitude CSMs are usually continuous and smooth, but the phase CSMs can show phase wraps (jumps from $-\pi$ to $+\pi$). These discontinuous phases can lead to interpolation errors, especially in the slice-direction where relatively few points of support are available. Therefore, the phase must be unwrapped before interpolation. In our study, the phase map of the first coil was chosen as a baseline. The sensitivity of each coil, including the first one, was then multiplied by the conjugate term of the baseline to achieve phase alignment.³⁹ After removing phase discontinuities, the real and imaginary components are interpolated separately and then combined. In the interpolation process, first the six degrees of freedom obtained from tracking camera coordinate system need to be translated to the 3D image matrix coordinate system by referencing the calibration of rotation matrix. Next, the Makima piecewise cubic Hermite method in MATLAB (<https://www.mathworks.com/help/matlab/ref/makima.html>) was used to interpolate the CSMs with the inverse of motion parameters. Finally, SMS reconstruction was performed using the updated CSMs C' .

3.2 | MRI experiments

MRI studies were performed on a 3 T whole-body system (MAGNETOM Prisma, version MR VE13C and VE11E, Siemens Healthcare) equipped with a 20-channel head coil. The product gradient-echo SMS-EPI sequence was

modified to receive motion parameters from the PMC system, and sequence parameter correction and receiver phase correction as per Eq. (4) were then performed in real time. All images were acquired in the axial plane.

3.2.1 | Prospective motion correction

Motion tracking was performed using four infrared cameras (Kineticor) mounted on top of the scanner bore. The camera system tracks the movement of a marker with an accuracy of 0.1 mm and 0.1° at 60 Hz frame rate. For each frame, the current pose (3 translations and 3 rotations) is sent via a user datagram protocol (UDP) packet to the scanner host computer and logged in the computer. A software on the scanner processes the incoming UDP motion packets and updates the rotation matrix and slice offsets in real time to keep scanning parameters aligned with the mobile reference frame of the brain (or phantom). The lag time between acquisition of an image by the cameras and corresponding motion update on the scanner was ~25–30 ms.

Motion updates and associated receiver phase adjustments were applied quasi-continuously during the EPI readout train, as follows. First, the receiver phase was adjusted in real-time at the start of each individual k-space line as a function of the current PE step number N_y and the latest slice translation update available (Eqs. [2–4]). However, because the PMC system generates motion updates approximately every 16.7 ms (frame rate 60/s), all k-space lines within a given 16.7 ms camera frame experience the same slice update Δz . More specifically, each EPI-train (e.g., length 46 ms) experienced an average of ~2.7 motion updates (46/16.7).

Of note, motion updates on the scanner were not corrected for the lag from the camera acquisition (actual movements). For this reason and because the tracking system is not synchronized with the MR acquisition, the exact timing of the “intra-train” motion updates cannot be predicted; however, the effect of the “intra-train” updates on the phase is still captured by Eq. (4).

3.2.2 | Phantom experiments

To test the real-time phase correction scheme (Eq. [4]), a spherical phantom without internal structure was placed inside the 20-channel head coil. The SMS-EPI scan parameters were TR/TE 3000/30 ms, flip angle 90°, FOV 280 × 280 mm², receiver bandwidth 2170 Hz/pixel, matrix size 64 × 64, slice thickness 5 mm, slice center-to-center distance 25 mm, 2 slices, SMS acceleration factor 2, and 30 repeats (scan time 90 s). The long TR provides more

signal relaxation, which can benefit image quality of the T₂-weighted scan. Single-slice reference images were acquired in a pre-scan using a single-band RF pulse and other EPI parameters identical to the SMS acquisition.

For initial testing, a custom program was used to inject UDP motion packages at 60 frames/s rate into the scanner to induce a 10-mm shift along slice direction approximately halfway through the scan. The PMC software reacts to this motion injection by shifting the slice positions by 10 mm, and the phase-correction algorithm needs to adjust the receiver phases (as per Eq. [4]) to eliminate phase-encoding ghosts. This experiment was performed twice: with and without real-time receiver phase correction. SP-SG was used to reconstruct the simultaneously acquired slices, using a kernel size of 5 × 5.

These experiments were repeated in a phantom with an internal structure using tracking markers, using identical scan parameters as above, except for the number of slices 16, slice center-to-center gap 10 mm and 20 repeats. The phantom was moved in a stepwise fashion starting at the 10th repetition, and the movements were primarily x-rotations (up to 20°) and z-translations (up to 50 mm). PMC was enabled, and the receiver phase was corrected in real time according to Eqs. (2–4). SENSE and SP-SG reconstructions were performed in MATLAB, using (1) data acquired in a stationary phantom; (2) motion data with original CSMs (oCSMs) and original SP-SG GRAPPA weights from single-slice reference data; and (3) motion data with updated CSMs (uCSMs) and updated GRAPPA weights for the new locations, calculated by interpolating oCSMs with the inverse of motion parameters.

Additionally, to quantify the performance of SENSE and SP-SG reconstruction with motion, simulations were performed using the raw data of the first repetition (stationary phantom). Movements were simulated by interpolating the original CSMs for 1 to 50 mm translations and 1° to 50° rotations (1 mm and 1° increments), and the interpolated CSMs were labeled simulated oCSMs (soCSMs). Using the no-motion images as a reference ($\mathbf{I}_{\text{reference}}$), PMC-induced signal deviations were quantified for reconstructed images ($\mathbf{I}_{\text{estimated}}$) using the cumulative normalized mean squared error ($cNMSE$)⁴⁰:

$$cNMSE = 100 \times \frac{\sum_{s=1}^N \sum_{\vec{r}} \left| \mathbf{I}_{\text{estimated}}^s(\vec{r}) - \mathbf{I}_{\text{reference}}^s(\vec{r}) \right|^2}{\sum_{\vec{r}} \left| \mathbf{I}_{\text{reference}}^s(\vec{r}) \right|^2}, \quad (14)$$

where \vec{r} denotes the voxel position, and N is the slice number. Interpolating the soCSMs with inverse motion parameters generated simulated uCSMs (suCSMs). The effects of motion correction were assessed by reconstructing the suCSMs with SENSE and SP-SG.

SENSE can be performed directly with CSMS, but new raw data had to be created for SP-SG to update the GRAPPA weights. The image of i^{th} individual coil is $\mathbf{m}_i = \mathbf{C}_i \mathbf{m}$, where \mathbf{C}_i is the sensitivity of the i^{th} coil, and \mathbf{m} is the magnetization that can be estimated by coil-combined image with sum-of-squares method. When motion occurs and PMC is enabled (i.e., FOV always follows the object in the presence of motion), the sum-of-squares image with motion is $\mathbf{m}' = \mathbf{m}_{\text{no-motion}}$, where $\mathbf{m}_{\text{no-motion}}$ is the sum-of-squares image before motion and is equal to $|\mathbf{I}_{\text{reference}}|$, where $|\mathbf{I}_{\text{reference}}|$ is coil-combined reference image. Therefore, the new k-space data for coil j is generated using

$$\mathbf{K}^{j'} = \mathcal{F}(|\mathbf{I}_{\text{reference}}| \mathbf{C}^{j'}), \quad (15)$$

where \mathcal{F} is Fourier transformation, and $\mathbf{C}^{j'}$ is the apparent coil sensitivity profile at coil j after motion. Next, updated GRAPPA weight coefficients can be obtained by feeding the new data into Eq. (12), which are then used for SMS reconstruction.

3.3 | In vivo experiments

To examine the effectiveness of the new SMS-EPI motion correction algorithms, three healthy volunteers (age 36 ± 7 years, two males, one female) were recruited. Written informed consent was received from each subject as approved by the local institutional review board. A tracking marker was attached to the nose of each volunteer so that the tracking system can capture the head movements and send position information to the scanner. Subjects

were trained to move their head in the 20-channel head coil. SMS-EPI scans were acquired as follows. Subject A: two, three and fourfold SMS acceleration factors (AFs); subject B: three and fourfold AFs; subject C: five and sixfold AFs. All scans had real-time receiver phase correction and PMC enabled. The scan parameters were TR/TE 3000/30 ms, fat suppression, slice thickness 5 mm with 5 mm gap, FOV $240 \times 240 \text{ mm}^2$, matrix size 84×84 , 30 repetitions. The number of slices was 16 (fourfold AF), 18 (sixfold), 20 (two and fivefold), and 21 (threefold). The first time point was used as no-motion reference. The scan time for each scan was 98 s.

Subject C completed another session to assess the effects of the EPI receiver phase correction (Eq. [4]) on the quality of an SMS “resting-state” acquisition with minimal head movements. Three scans were acquired using a slightly modified United Kingdom Biobank fMRI protocol: slice thickness 2.4 mm without gap, FOV $210 \times 210 \text{ mm}^2$, TR/TE 735/39 ms, fat suppression, SMS AF 8, matrix size 88×88 , bandwidth 2030 Hz/pixel, repeats 332, scan time 244 s. The number of slices was reduced from 64 to 48 (number of SMS excitations per TR from 8 to 6) to eliminate an instability caused by our prototype motion-corrected SMS sequence. The Biobank protocols can be found at https://www.fmrib.ox.ac.uk/ukbiobank/protocol/V4_23092014.pdf. During all three scans, the subject was instructed to cross legs every 22 s to induce small yet relatively reproducible head movements. The first scan was acquired without any motion correction. For the second scan, PMC was enabled but receiver phase correction was OFF, and for the third scan, both PMC and receiver phase corrections were ON.

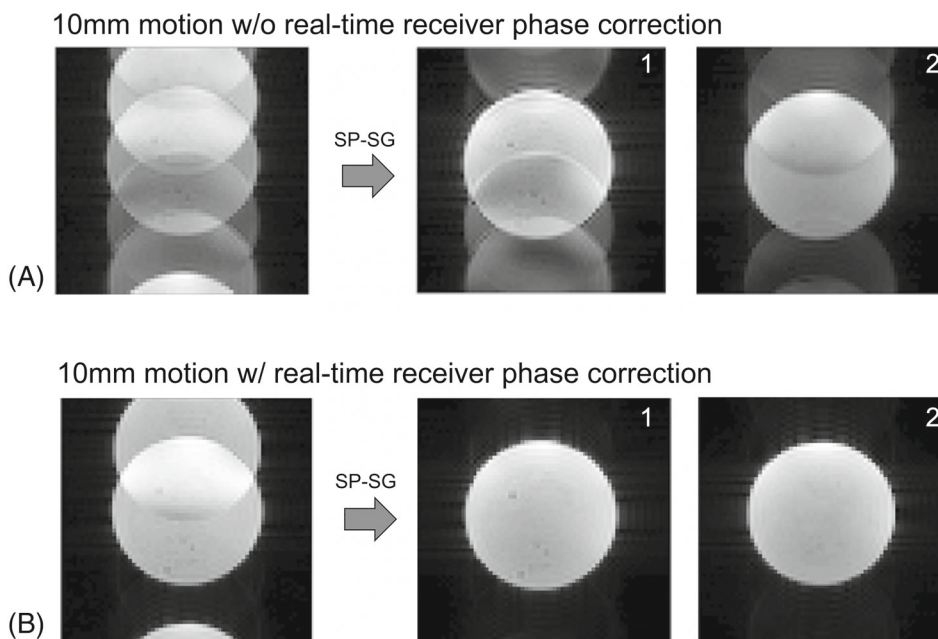


FIGURE 1 Images without (A) and with (B) real-time receiver phase correction, after injecting a 10 mm slice offset into the simultaneous multislice (SMS)-EPI sequence. The left column shows the aliased images of two simultaneously acquired slices with FOV/4 blipped-controlled aliasing in parallel imaging (CAIPI) interslice shift. The center and right columns show the split slice-GRAPPA (SP-SG) reconstructions of the two simultaneously excited slices. The aliasing artifacts are eliminated by updating the receiver phases in real time. Numbers in the top right corners indicate slice numbers.

3.4 | Analysis of in vivo data

Because all in vivo scans involved EPI time series while subjects performed head movements, the temporal signal to noise ratio (tSNR) was used as a measure of temporal

stability of signals. The tSNR for each voxel was obtained by dividing the mean of the voxel time series by its standard deviation. Preprocessing included slice-by-slice alignment of the time-course images and smoothing with a Gaussian kernel ([1] pixel size; SPM 12). A foreground masking

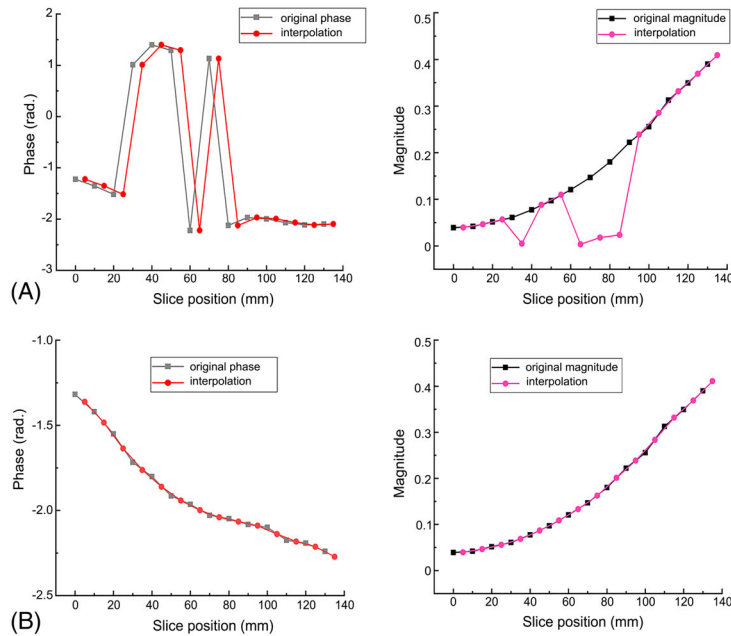
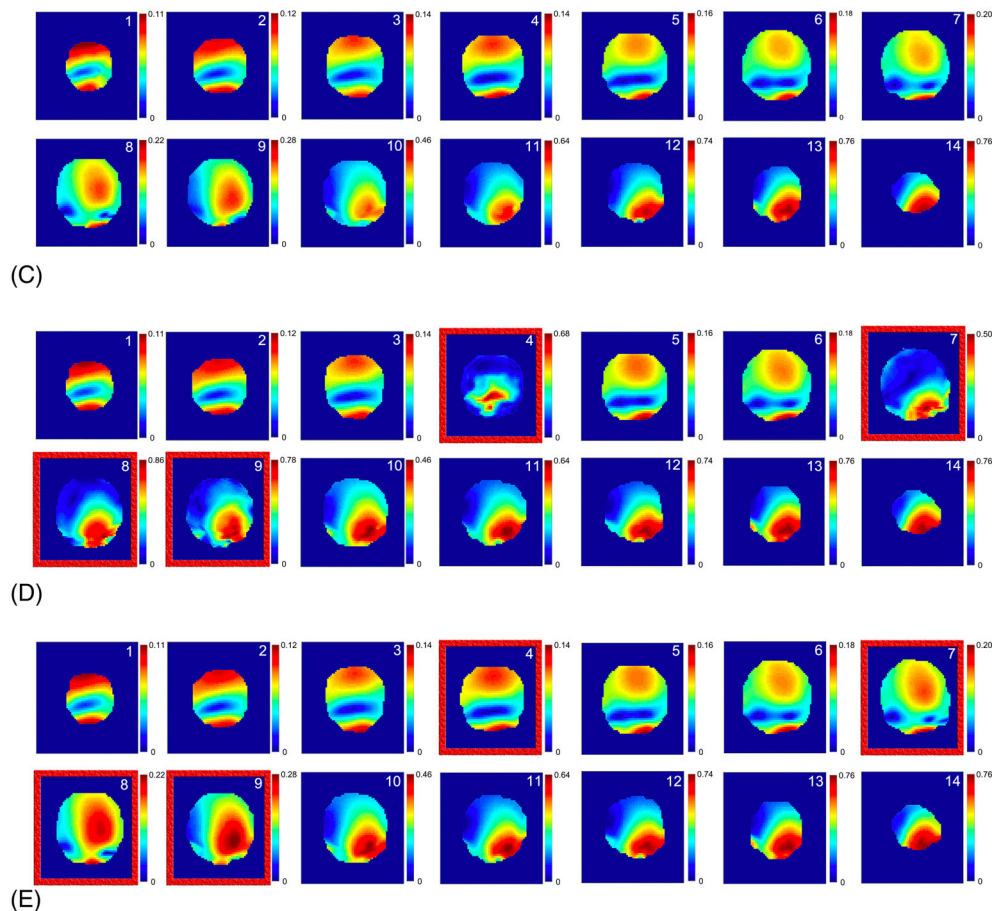


FIGURE 2 Results of interpolations across slices using wrapped (original) phases (A,D) and the corrected phase (B,E) with 5 mm z translation. The simulation has 14 slices at 0–130 mm z positions with 5-mm slice thickness and 10 mm center-to-center gap. The phases and magnitudes with wrapped and corrected phase at image center point of each slice are plotted in (A) and (B). The gray and black dots and lines represent the phases and magnitudes of measured data. Each dot represents a slice. The red and magenta dots and lines represent the interpolated phases and magnitudes with 5 mm translation along slice-select direction. The original coil sensitivity maps (CSMs) used for the 5 mm interpolation are shown in (C). The color map of interpolated CSMs with wrapped and corrected phase are shown in (D) and (E). Numbers in the top right corners in maps indicate slice positions.



algorithm was then used to exclude all background voxels,⁴¹ and slices containing no brain or small brain volume were excluded for the tSNR calculation. For each scan, the mean tSNR value was calculated by averaging tSNR values from foreground-masked image volumes across all slices. Therefore, two sets of seven tSNR values were obtained, one each for reconstruction with oCSMs and uCSMs. A paired t-test was performed to compare tSNR changes between oCSMs and uCSMs (for the 2*7 means), and a *p*-value <0.05 was considered significant.

4 | RESULTS

4.1 | Real-time receiver phase correction

Figure 1 shows phantom results for two simultaneously acquired slices without (Figure 1A) and with (Figure 1B) real-time receiver phase correction, after injecting a 10 mm slice offset into the SMS-EPI sequence. The left column shows the aliased images of two simultaneously acquired slices with FOV/4 blipped-CAIPI interslice shift. Shifting

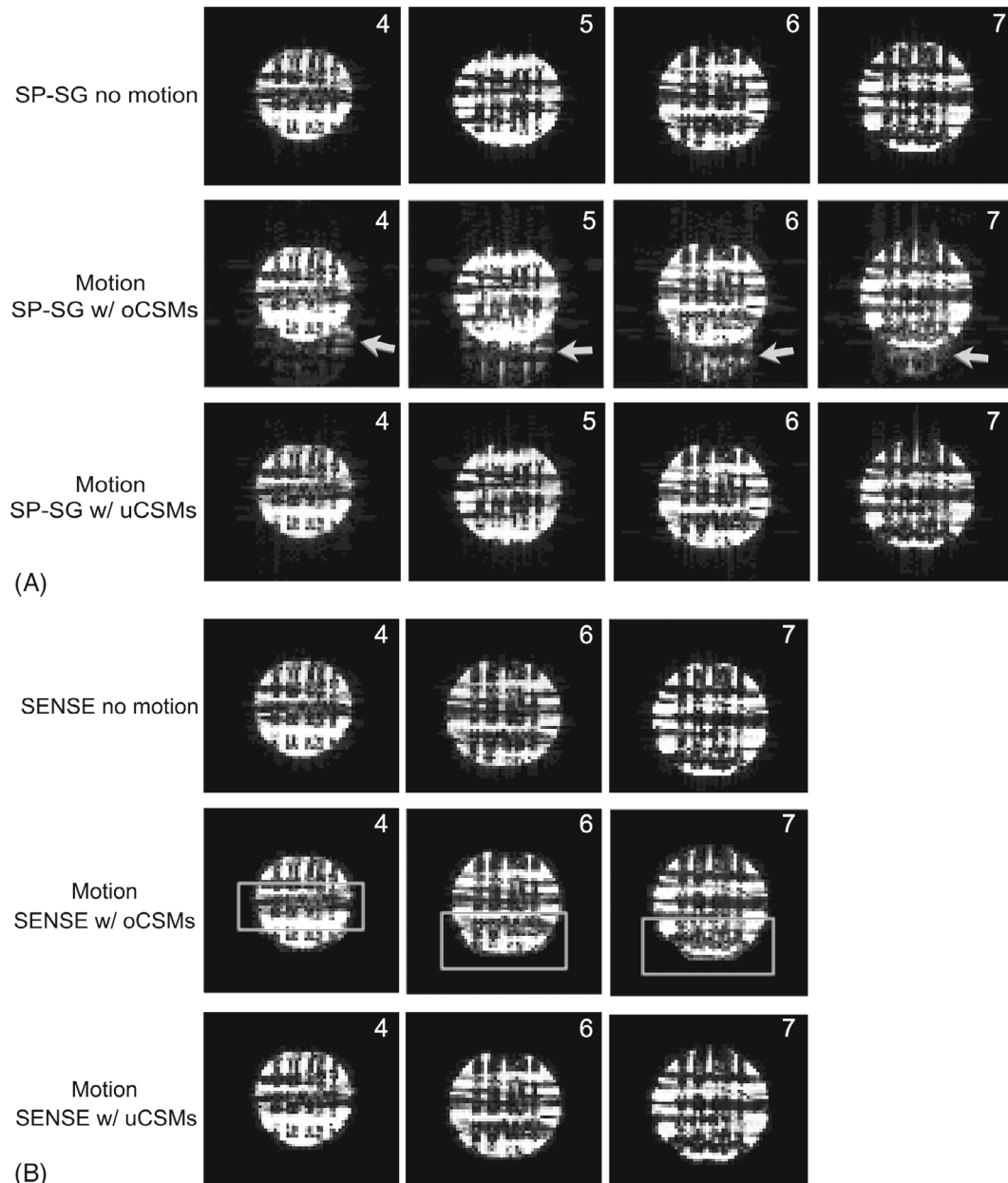


FIGURE 3 Simultaneous multislice (SMS)-EPI reconstruction using split slice-GRAPPA (SP-SG) (A) and SENSE (B) with original coil sensitivity maps (oCSMs) and updated coil sensitivity maps (uCSMs) after movement of x/y/z-translation $-2.4/6.4/21.5$ mm and x/y/z-rotation $10.5^\circ/5.2^\circ/-0.5^\circ$. Aliasing artifacts appear in the SP-SG with oCSMs, as shown by gray arrows in (A). SENSE images with oCSMs show artifacts (gray boxes in B). Numbers in the top right corners indicate slice positions.

the slices by 10 mm without phase correction causes severe aliasing artifacts in the individual images (Figure 1A, center and right columns). Conversely, the aliasing artifacts are eliminated when the receiver phase is corrected during acquisition (Figure 1B).

4.2 | Interpolation of CSMs

Figure 2 shows the phase and magnitude of the coil sensitivity profiles for a single RF coil across several slices. The original magnitude values across slices are smooth, as shown by black dots and lines in Figure 2A right. Each dot represents the image center point of each slice. However, the phase shows 2π jumps across some slices (e.g., slices 4, 5, 6, and 8; gray dots in Figure 2A left column), causing discontinuities in both interpolated phases and magnitudes (red and magenta dots and lines in Figure 2A). In contrast, when the phase is unwrapped, the phases as well as magnitudes of interpolated data are continuous (Figure 2B, red and magenta dots and lines).

Likewise, compared to the original CSMs (Figure 2C), several CSMs interpolated without phase unwrapping exhibit large changes in magnitude for a 5 mm shift

(Figure 2D; 10 mm center-to-center distance; slices 4, 7, 8, and 9 with red frames). Interpolation with the unwrapped phase removes these magnitude errors in CSMs across slices (red framed slices in Figure 2E).

4.3 | Moving phantom

Figure 3 demonstrates the effects of motion-induced FOV changes on SP-SG and SENSE reconstructions when PMC is enabled. The motion primarily involved an x-rotation (x/y/z-rotations $10.5^\circ/5.2^\circ/-0.5^\circ$) and z-translation (x/y/z-translations $-2.4/6.4/21.5$ mm). SP-SG reconstructions using oCSMs show residual aliasing artifacts (arrows in Figure 3A, middle row) that obscure some inner structures and outer boundaries. The corresponding SENSE reconstructions are shown in Figure 3B. Again, reconstructions with oCSMs show some aliasing artifacts (gray boxes), although artifacts are less severe compared to the SP-SG reconstructions. Conversely, the inner structure and boundaries for both reconstructions are well delineated when uCSMs (interpolated to account for apparent coil movements) are used, and aliasing artifacts are eliminated (bottom row in Figure 3A,B).

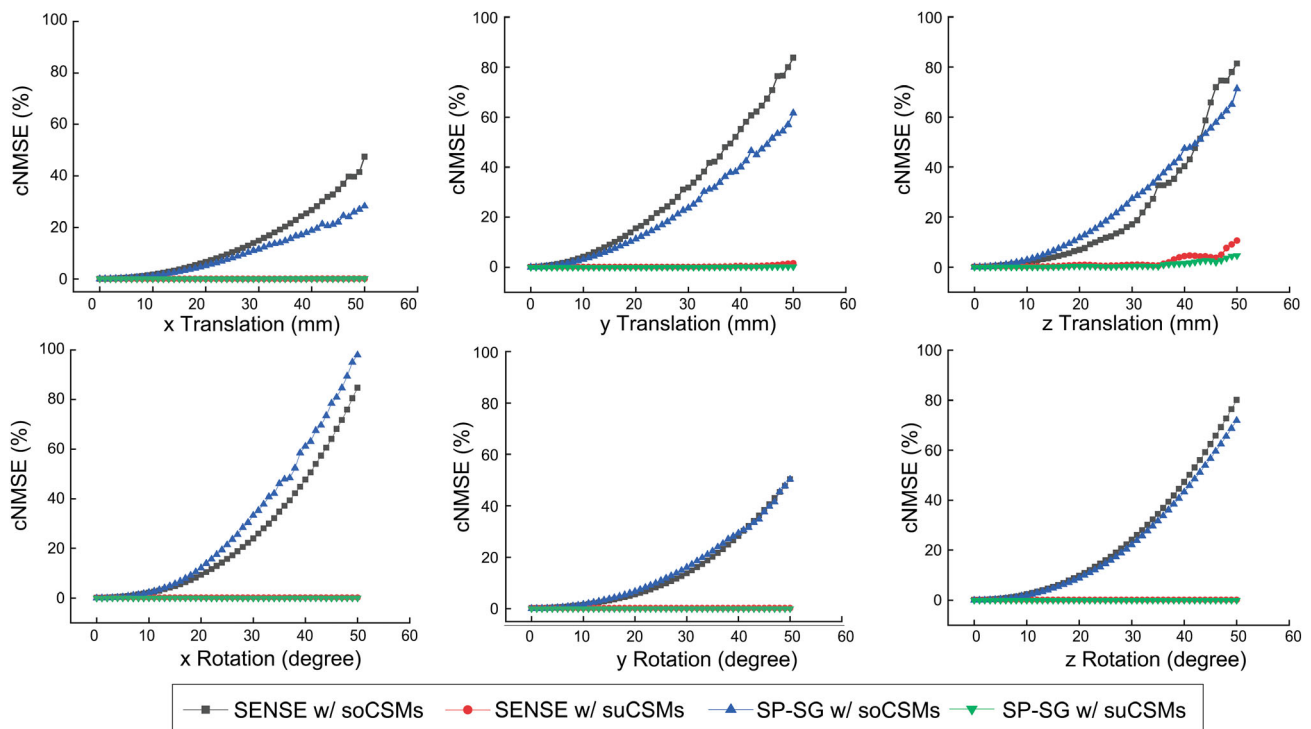


FIGURE 4 The cumulative normalized mean squared errors (cNMSEs) for SENSE and split slice-GRAPPA (SP-SG) with simulated translations of 1–50 mm and rotations of 1° – 50° , plotted against the amplitude of motion. Each plot represents one motion degree of freedom. The cNMSEs with simulated updated coil sensitivity maps (suCSMs) show only minimal dependence on motion parameters (red curves for SENSE and green curves for SP-SG), whereas the errors rise continuously when simulated original coil sensitivity maps (soCSMs) are used for reconstruction (black and blue curves for SENSE and SP-SG).

These qualitative findings are supported by analyses using the cNMSEs as a function of simulated translations (Figure 4, top row) and rotations (Figure 4, bottom row). When soCSMs are used during these simulated movements, the cNMSEs show a continuous, second or higher-order increase with the amplitude of translations or rotations for both SENSE and SP-SG reconstructions (black and blue curves in all plots). Conversely, the

cNMSEs of images reconstructed with suCSMs generally show only minimal increases with motion parameters (red curves for SENSE and green curves for SP-SG), up to 40 to 50 mm or degrees. However, for larger z translations (over 35 mm), SP-SG and especially SENSE reconstructions show some increases and fluctuations in cNMSEs, although errors remain substantially below those using soCSMs.

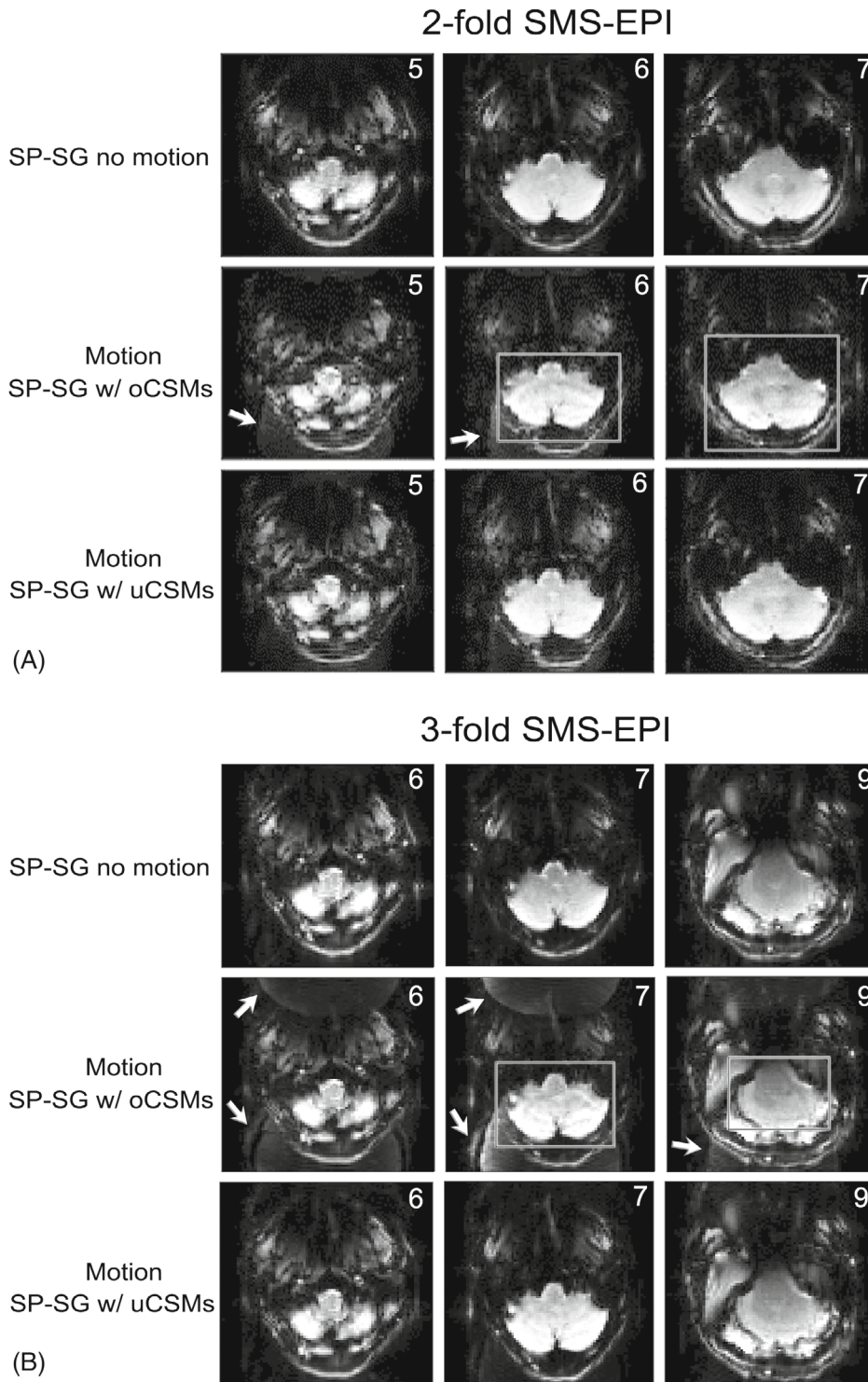


FIGURE 5 Split slice-GRAPPA (SP-SG) reconstructions for subject A with no motion (reference; top row), and reconstructions with motion and original coil sensitivity maps (oCSMs) (middle row) or updated CSMs (uCSMs) (bottom row). (A) Images were acquired with the twofold simultaneous multislice (SMS)-EPI sequence. The motion parameters are $x/y/z$ -translation 3.8/7.3/20 mm and $x/y/z$ -rotation $-7.4^\circ/1.1^\circ/6.7^\circ$. (B) Images were acquired with threefold SMS-EPI. The motion parameters are $x/y/z$ -translation 0.8/3.7/14.4 mm and $x/y/z$ -rotation $-3.8^\circ/0.6^\circ/3.0^\circ$. Images reconstructed with oCSMs show residual aliasing artifacts (middle row; white arrows), and ripple artifacts in the cerebellum (gray boxes). These artifacts are substantially reduced for images reconstructed with uCSMs (bottom row). Numbers in the top right corners indicate slice positions.

4.4 | In vivo studies

Figure 5 shows SP-SG reconstructions of subject A scans with twofold (Figure 5A) and threefold (Figure 5B) slice accelerations using oCSMs and uCSMs. For both scans, the predominant movement was a z-translation (20 and 14 mm for Figure 5A,B). First, it is apparent that the PMC system retained the position of slices relative to the no-motion images (top row). However, reconstructions

with oCSMs cause residual aliasing artifacts (middle row, white arrows). The bleed-through from other slices was especially pronounced for the scan with threefold acceleration (e.g., slice 7 in Figure 5B). Additionally, the oCSM reconstructions show banding artifacts in the cerebellum (gray boxes) compared to the no-motion scan. These artifacts are substantially reduced when uCSMs are used for reconstruction instead of oCSMs (Figure 5A,B, bottom row), although some minor artifacts remained.

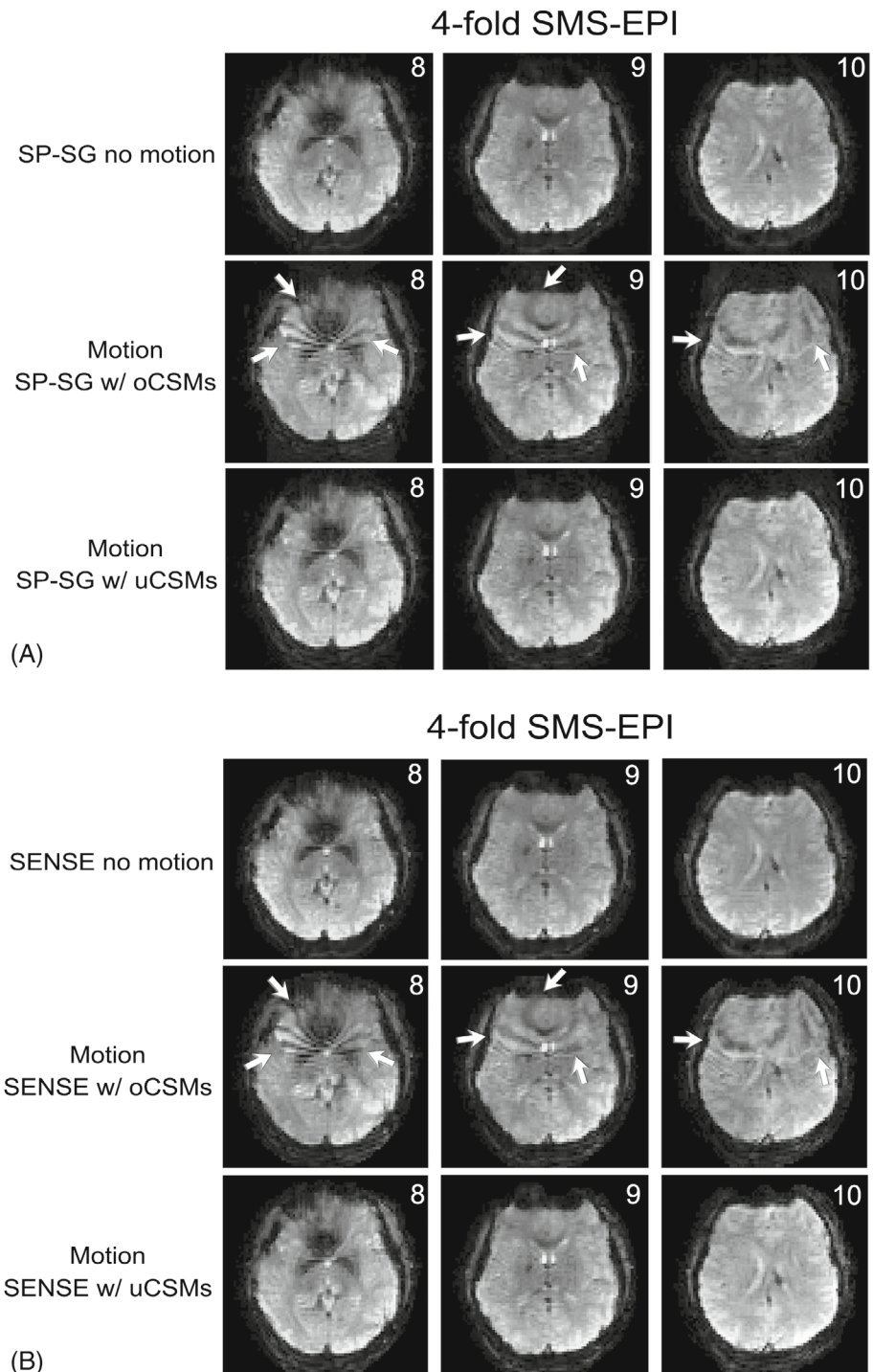


FIGURE 6 Simultaneous multislice (SMS)-EPI images reconstructed with original coil sensitivity maps (oCSMs) and updated CSMs (uCSMs) at fourfold accelerated acquisition for subject B. The images in (A) and (B) are reconstructed using split slice-GRAPPA (SP-SG) and SENSE, respectively. The motion parameters are x/y/z-translation 3.8/1.4/0.9 mm and x/y/z-rotation 0.3°/4.5°/26.1°. Noticeable aliasing artifacts can be seen in the images reconstructed with oCSMs in the middle row (white arrows). These artifacts are eliminated in the images reconstructed with uCSMs (bottom row). Numbers in the top right corners indicate slice positions.

A head-to-head comparison between an SP-SG and SENSE reconstruction of a scan with fourfold slice acceleration is shown in Figure 6 (subject B). Notably, SP-SG and SENSE reconstructions with uCSMs show similar image quality, and both show pronounced ripple artifacts (middle row, white arrows in Figure 6A,B) in the brain with oCSM reconstructions (especially slice 8). Despite the relatively

large z-rotation involved (26.1°), slice bleed-through was relatively minor on both oCSM reconstructions. Again, the artifacts in oCSM reconstructions are mostly eliminated when uCSMs were used (bottom row in Figure 6A,B).

Figure 7 shows SP-SG reconstructions for subject C with yet higher accelerations (fivefold; Figure 7A and sixfold; Figure 7B). The movement was predominantly a

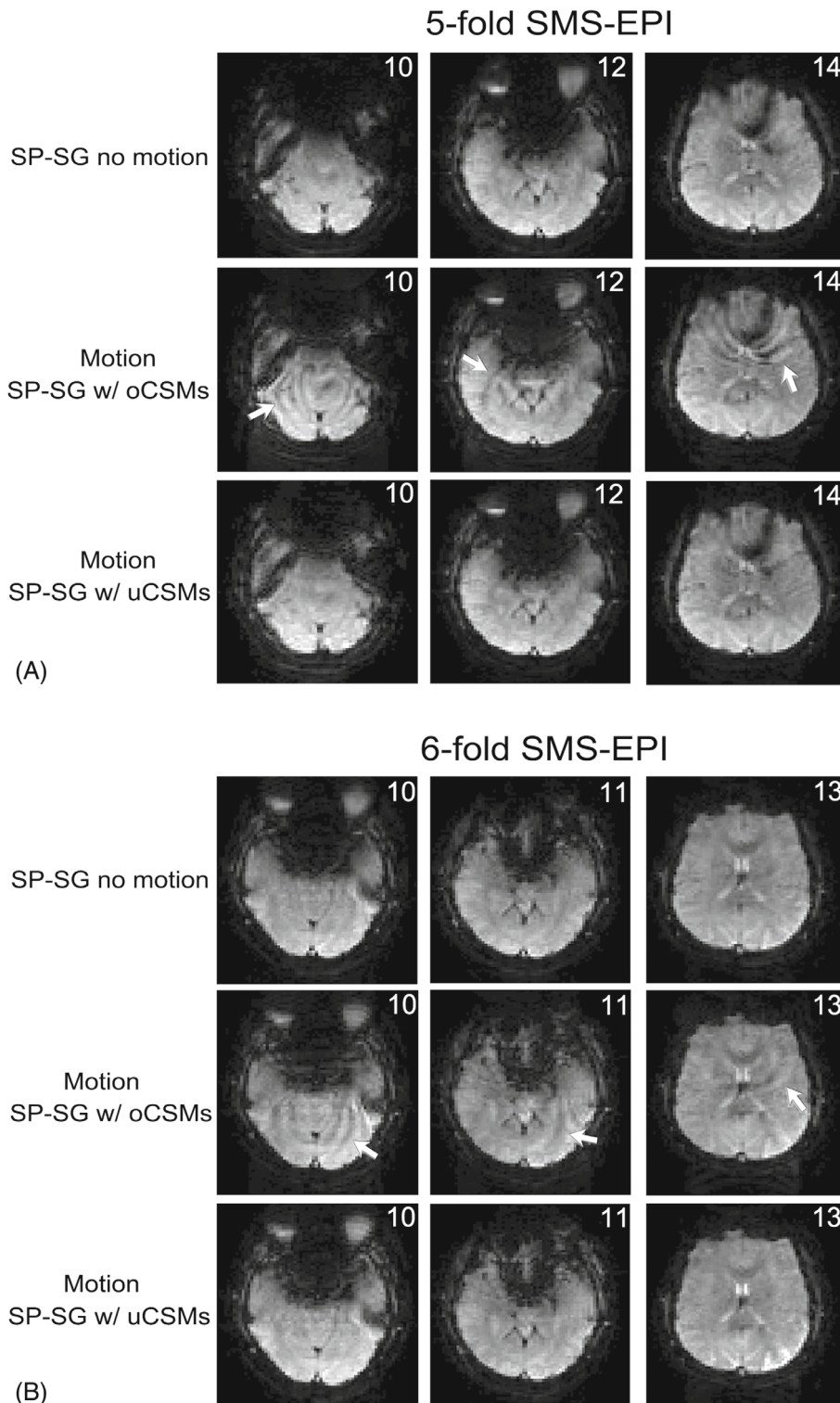


FIGURE 7 Split slice-GRAPPA (SP-SG) reconstructions for subject C with fivefold simultaneous multislice (SMS)-EPI acquisition (A) and sixfold acquisition (B). The movements were primarily z-rotation: (A) x/y/z-translation $-2.2/-0.8/0.6$ mm and x/y/z-rotation $-1.2^\circ/-2.5^\circ/-16.8^\circ$; (B) x/y/z-translation $5.0/1.2/0.4$ mm and x/y/z rotation $0.7^\circ/1.3^\circ/14.3^\circ$. Reference images were acquired with no motion (top row). Images reconstructed with original coil sensitivity maps (oCSMs) show ripple aliasing artifacts (middle row; white arrows). These artifacts are substantially removed for images reconstructed with updated CSMs (uCSMs) (bottom row). Numbers in the top right corners indicate slice positions.

TABLE 1 Mean tSNR comparison between reconstructions with oCSMs and uCSMs for in vivo experiments.

Subjects	SMS acceleration factor	tSNR with oCSMs	tSNR with uCSMs	Translation (mm)	Rotation (°)
A	2	40.39	42.77	-7 to 24.3	-13.6 to 26.1
	3	28.57	39.19	-2.7 to 23.7	-7.6 to 24.6
	4	30.18	36.72	-5.5 to 15.7	-14.5 to 19.8
B	3	22.15	27.47	-6.1 to 31.5	-30.0 to 25.0
	4	17.15	21.92	-7.4 to 35.1	-27.8 to 26.7
C	5	19.20	24.66	-4.3 to 36.6	-22.4 to 3.3
	6	18.47	24.94	-2.0 to 28.3	-2.5 to 24.7
	Mean \pm SD	25.16 \pm 8.39	31.10 \pm 8.27		
	<i>p</i> value	<i>p</i> = 0.0007			

Abbreviations: oCSMs, original coil sensitivity maps; SMS, simultaneous multislice; tSNR, temporal SNR; uCSM, updated coil sensitivity maps.

z-rotation (16.8° and 14.3° for Figure 7A,B). Again, compared to reference images with no motion (top row in Figure 7A,B), images reconstructed with oCSMs show ripple aliasing artifacts (middle row; white arrows). These artifacts are substantially attenuated in images reconstructed with uCSMs (bottom row).

Table 1 shows the mean tSNR values for reconstructions with oCSMs and uCSMs for all acceleration factors and subjects studied (total 2*7 scans). The mean (\pm SD) tSNR values were 25.16 \pm 8.39 for the reconstructions with oCSMs, compared to 31.10 \pm 8.27 for reconstructions with uCSMs. Therefore, the reconstruction with uCSMs improved the mean tSNR by 24% ($p = 0.0007$). Figure 8 shows the tSNR maps for subject C with sixfold slice acceleration. The tSNR maps with oCSMs (Figure 8A) show substantially more areas with low values than those with uCSMs (Figure 8B). The mean tSNR values are 18.47 and 24.94 for oCSMs and uCSMs, respectively.

Finally, representative tSNR maps from the three acquisitions with minimal motion (leg-crossing) are shown in Figure 9. The average tSNR was 75.3 for the scan with no motion correction (Figure 9 left column). The tSNR was essentially the same for the study with both PMC and receiver phase correction (RPC) enabled (tSNR = 74.1; Figure 9 right column), but was markedly reduced when RPC was omitted (tSNR = 49.5; Figure 9 center column).

5 | DISCUSSION

This study addressed two sources of image artifacts in SMS-EPI when subjects move while PMC is enabled: uncorrected receiver phase changes during the EPI readout train and coil sensitivity mismatch between the reference and updated slice locations. To eliminate the first source of artifacts, the receiver phase was adjusted in real-time for each k-space line during the EPI readout

train. To eliminate artifacts caused by the misregistration of coil sensitivity after motion updates, SMS reconstructions were performed with updated (interpolated) coil sensitivity profiles, which reflect actual location. Phantom and in vivo experiments demonstrate that the proposed measures can substantially attenuate aliasing artifacts from scans acquired with large movements, and correcting coil sensitivity profiles during SMS reconstruction significantly improved tSNR values.

An SMS resting-state scan with minimal motion acquired with PMC enabled showed substantial reductions in tSNR when the real-time receiver phase correction was omitted. In this scenario, minimal head movements can induce subtle ghost artifacts when SMS slice positions, but not receiver phases, are updated across TR periods. Because the tSNR for the scan without motion correction was relatively high (~ 75), even small (< 1 mm) translations in slice direction can cause a substantial drop in tSNR without receiver phase correction. However, enabling phase correction eliminated the artifacts and consequently reversed the reduction in tSNR.

In simulations, SP-SG and SENSE reconstructions using oCSMs showed similar and essentially quadratic increases in reconstruction errors with motion amplitudes. Using uCSMs markedly reduced errors even for large rotations and translations of up to 50° and 50 mm. The somewhat reduced effectiveness of corrections for large z-translations may be caused by the limited number of support points in slice direction and the resulting need to extrapolate coil profiles, which are likely less accurate than interpolations. The somewhat better performance of SP-SG for large translations (> 35 mm) suggests that SENSE may be more sensitive to regional CSM alterations. In contrast, GRAPPA-based approaches estimate missing data based on global information,⁴² which may make SP-SG more robust to regional CSM alterations than SENSE.

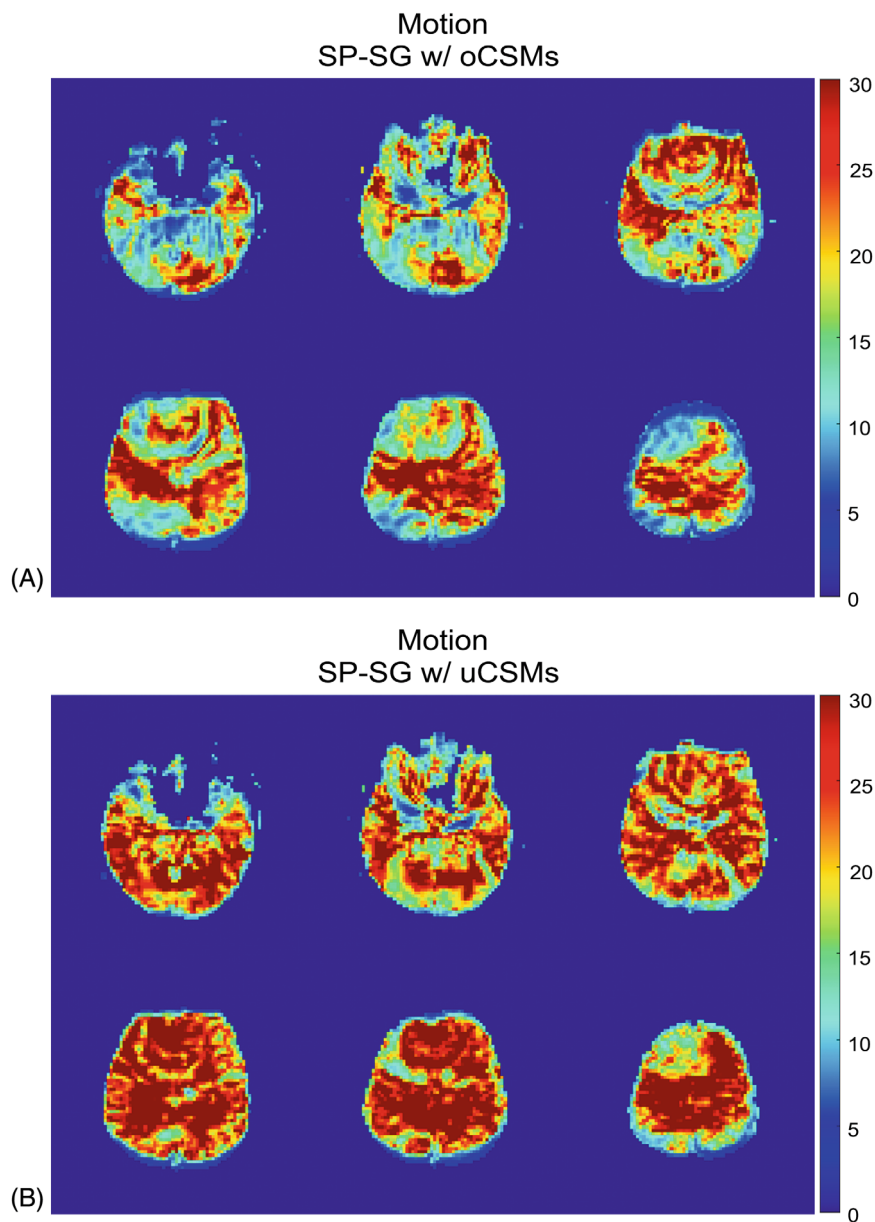


FIGURE 8 Temporal SNR (tSNR) maps for subject C with sixfold slice acceleration. The tSNR maps with original coil sensitivity maps (oCSMs) (A) show substantially more areas with low values than those with updated CSMs (uCSMs) (B). The translation during the scan was -2.0 to 28.3 mm, and the rotation was -2.5° to 24.7° . The mean tSNR values are 18.47 and 24.94 for oCSMs and uCSMs, respectively. The images used for the tSNR calculation were reconstructed by split slice-GRAPPA (SP-SG).

Updated coil sensitivity values were calculated using the Makima piecewise cubic Hermite algorithm, which uses low-order polynomials and makes interpolation results smooth, consistent with the overall behavior of CSMs. To satisfy another important property of CSMs (i.e., continuity), phase alignment was performed for all coil channels by choosing the first coil channel as a baseline. Both phantom and in vivo experiments demonstrate that the combination of Makima interpolation and phase alignment can provide relatively accurate CSM interpolation in the presence of motion, leading to a marked reduction in artifacts when using the interpolated CSMs for reconstructions.

Ideally, updated CSMs could be measured dynamically by reacquiring single-slice reference images at new positions. However, reacquiring reference images is

challenging because these reacquisitions would disturb the steady state of the main acquisition and obviously increase scan times. Another approach to obtain uCSMs would be to record a library of CSMs at various head positions before scan. However, this would require the willingness and ability of subjects to engage in predefined head movements as per the scanner operator's instructions.

We used an MR-compatible optical system to track head motion with high precision and a high frame rate. These optical and other external tracking systems still have limited availability, and MR-based navigators can also track head motion for PMC, both for structural MRI^{25,28,43–45} and single-shot time series.^{46,47} However, the proposed methods to eliminate phase and CSM alterations when PMC is enabled only require accurate information on the motion state at the beginning of each

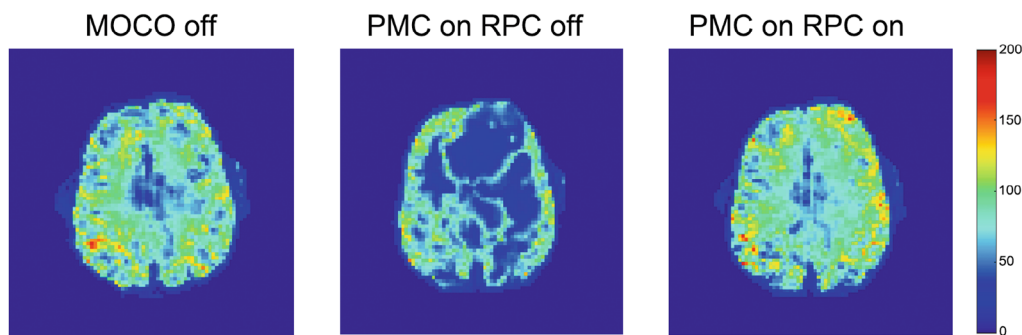


FIGURE 9 Representative “resting-state” temporal signal to noise ratio (tSNR) maps for scans with three settings of real-time corrections. Left: motion correction (MOCO) off. Center: prospective motion correction (PMC) on, but receiver phase correction (RPC) off. Right: both PMC and RPC on. Data were acquired with eightfold slice acceleration, and the subject was instructed to cross legs approximately every 22 s. The tSNR map with PMC on and RPC off (center column) shows substantial reductions in tSNR compared to the scans with both PMC and RPC on (right column) and MOCO off (left column).

SMS excitation. Therefore, our methods should work in conjunction with all tracking approaches, including non-optical ones.

Our study has several limitations. First, we only studied slice (through-plane) acceleration. Reconstruction artifacts because of in-plane acceleration or combinations of in-plane and through-plane acceleration were not evaluated. Second, the accuracy of CSM estimates beyond measured areas of support (i.e., extrapolation) is likely to be compromised for large movements. Although this issue did not appear to be a major problem in our study, better extrapolation methods may improve the accuracy of reconstructions. Third, our study used standard multiband SENSE reconstruction, which may result in Nyquist-ghost signals when simultaneously excited slices require different phase correction during reconstruction.^{48,49} Although we did not observe residual ghosts in our data, combining the methods presented with those to reduce residual Nyquist-ghosts might further improve the quality of scans acquired during motion with PMC enabled. Finally, the tSNR values observed in our study are lower than typical values of 100:1 for BOLD fMRI-studies. This reduction in tSNR is most likely a result of the rather large movements used (30° range), which induce B_0 changes and spatial distortions that were not fully corrected.

6 | CONCLUSION

The blipped SMS-EPI was modified to implement motion correction for single-shot EPI acquisitions. Updated receiver phase and coil sensitivity profiles were used to eliminate aliasing artifacts caused by position changes. Correcting the receiver phase in real time and updating coil sensitivity profiles during reconstruction substantially reduced artifacts for both SP-SG and SENSE reconstructions and markedly increased the tSNR of time

series. Our method may be a valuable tool to improve the quality of SMS-EPI acquisitions in subjects who are prone to movements, for instance, young children, patients with dementia, or those who are confused or agitated.

ACKNOWLEDGMENTS

This work was supported by National Institutes of Health (NIH) grant R01 DA021146 (Bioengineering Research Partnership). R.B. was supported in part by National Science Foundation grant DMS-2108900 and Simons Foundation Fellowship grant 818333. Z.W was supported by NIH grants R01AG060054; R01AG070227; R01EB031080-01A1; P41EB029460-01A1; R21AG082435; and 1UL1TR003098. We acknowledge Drs. Pan Su and Tobias Kober from Siemens Healthineers for providing technical assistance and expertise. We also thank Dr. Yiran Li for helpful discussions on fMRI.

CONFLICT OF INTEREST STATEMENT

T.E. is an advisor to and owns equity in Kineticor.

DATA AVAILABILITY STATEMENT

Source code for the entire reconstruction as well as some of the examples in this article are available at https://github.com/MRIMoCo/SMS_EPI_MOCO.

ORCID

Bo Li  <https://orcid.org/0000-0002-0388-1574>

Radu Balan  <https://orcid.org/0000-0002-6217-3236>

Thomas Ernst  <https://orcid.org/0000-0003-1211-7655>

REFERENCES

1. Mansfield P. Multi-planar image formation using NMR spin echoes. *Jphys C: Solid State Phys.* 1977;10:L55-L58.
2. Feinberg DA, Moeller S, Smith SM, et al. Multiplexed echo planar imaging for sub-second whole brain FMRI and fast diffusion imaging. *PLoS One.* 2010;5:e15710.

3. Sanchez-Panchuelo RM, Besle J, Beckett A, Bowtell R, Schluppeck D, Francis S. Within-digit functional parcellation of Brodmann areas of the human primary somatosensory cortex using functional magnetic resonance imaging at 7 tesla. *J Neurosci*. 2012;32:15815-15822.
4. Poplawsky AJ, Fukuda M, Murphy M, Kim SG. Layer-specific fMRI responses to excitatory and inhibitory neuronal activities in the olfactory bulb. *J Neurosci*. 2015;35:15263-15275.
5. Le Ster C, Moreno A, Mauconduit F, et al. Comparison of SMS-EPI and 3D-EPI at 7T in an fMRI localizer study with matched spatiotemporal resolution and homogenized excitation profiles. *PLoS One*. 2019;14:e0225286.
6. Hoinkiss DC, Erhard P, Breutigam NJ, von Samson-Himmelstjerna F, Günther M, Porter DA. Prospective motion correction in functional MRI using simultaneous multislice imaging and multislice-to-volume image registration. *Neuroimage*. 2019;200:159-173.
7. Faraji-Dana Z, Tam F, Chen JJ, Graham SJ. A robust method for suppressing motion-induced coil sensitivity variations during prospective correction of head motion in fMRI. *Magn Reson Imaging*. 2016;34:1206-1219.
8. Gati JS, Menon RS, Ugurbil K, et al. Experimental determination of the BOLD field strength dependence in vessels and tissue. *Magn Reson Med*. 1997;38:296-302.
9. Barth M, Breuer F, Koopmans PJ, Norris DG, Poser BA. Simultaneous multislice (SMS) imaging techniques. *Magn Reson Med*. 2016;75:63-81.
10. Larkman DJ, Hajnal JV, Herlihy AH, Coutts GA, Young IR, Ehnholm G. Use of multicoil arrays for separation of signal from multiple slices simultaneously excited. *J Magn Reson Imaging*. 2001;13:313-317.
11. Moeller S, Yacoub E, Olman CA, et al. Multiband multislice GE-EPI at 7 tesla, with 16-fold acceleration using partial parallel imaging with application to high spatial and temporal whole-brain fMRI. *Magn Reson Med*. 2010;63:1144-1153.
12. Feinberg DA, Vu AT, Beckett A. Pushing the limits of ultra-high resolution human brain imaging with SMS-EPI demonstrated for columnar level fMRI. *Neuroimage*. 2018;164:155-163.
13. Chiew M, Miller KL. Improved statistical efficiency of simultaneous multi-slice fMRI by reconstruction with spatially adaptive temporal smoothing. *Neuroimage*. 2019;203:116165.
14. Godenschweger F, Kagebein U, Stucht D, et al. Motion correction in MRI of the brain. *Phys Med Biol*. 2016;61:R32-R56.
15. Lee CC, Jack CR Jr, Grimm RC, et al. Real-time adaptive motion correction in functional MRI. *Magn Reson Med*. 1996;36:436-444.
16. Rohde GK, Barnett AS, Basser PJ, Marengo S, Pierpaoli C. Comprehensive approach for correction of motion and distortion in diffusion-weighted MRI. *Magn Reson Med*. 2004;51:103-114.
17. Andersson JL, Skare S. A model-based method for retrospective correction of geometric distortions in diffusion-weighted EPI. *Neuroimage*. 2002;16:177-199.
18. Dong Z, Wang F, Ma X, Dai E, Zhang Z, Guo H. Motion-corrected k-space reconstruction for interleaved EPI diffusion imaging. *Magn Reson Med*. 2018;79:1992-2002.
19. Maclaren J, Herbst M, Speck O, Zaitsev M. Prospective motion correction in brain imaging: a review. *Magn Reson Med*. 2013;69:621-636.
20. Zaitsev M, Dold C, Sakas G, Hennig J, Speck O. Magnetic resonance imaging of freely moving objects: prospective real-time motion correction using an external optical motion tracking system. *Neuroimage*. 2006;31:1038-1050.
21. Maclaren J, Armstrong BS, Barrows RT, et al. Measurement and correction of microscopic head motion during magnetic resonance imaging of the brain. *PLoS One*. 2012;7:e48088.
22. Kober T, Gruetter R, Krueger G. Prospective and retrospective motion correction in diffusion magnetic resonance imaging of the human brain. *Neuroimage*. 2012;59:389-398.
23. Engstrom M, Martensson M, Avventi E, et al. Collapsed fat navigators for brain 3D rigid body motion. *Magn Reson Imaging*. 2015;33:984-991.
24. Alhamud A, Tisdall MD, Hess AT, Hasan KM, Meintjes EM, van der Kouwe AJW. Volumetric navigators for real-time motion correction in diffusion tensor imaging. *Magn Reson Med*. 2012;68:1097-1108.
25. Tisdall MD, Hess AT, Reuter M, Meintjes EM, Fischl B, van der Kouwe AJW. Volumetric navigators for prospective motion correction and selective reacquisition in neuroanatomical MRI. *Magn Reson Med*. 2012;68:389-399.
26. Gallichan D, Marques JP. Optimizing the acceleration and resolution of three-dimensional fat image navigators for high-resolution motion correction at 7T. *Magn Reson Med*. 2017;77:547-558.
27. Huang P, Carlin JD, Alink A, Kriegeskorte N, Henson RN, Correia MM. Prospective motion correction improves the sensitivity of fMRI pattern decoding. *Hum Brain Mapp*. 2018;39:4018-4031.
28. van der Kouwe AJ, Benner T, Dale AM. Real-time rigid body motion correction and shimming using cloverleaf navigators. *Magn Reson Med*. 2006;56:1019-1032.
29. Ward HA, Riederer SJ, Grimm RC, Ehman RL, Felmlee JP, Jack CR. Prospective multiaxial motion correction for fMRI. *Magn Reson Med*. 2000;43:459-469.
30. Callaghan MF, Josephs O, Herbst M, Zaitsev M, Todd N, Weiskopf N. An evaluation of prospective motion correction (PMC) for high resolution quantitative MRI. *Front Neurosci*. 2015;9:97.
31. Speck O, Hennig J, Zaitsev M. Prospective real-time slice-by-slice motion correction for fMRI in freely moving subjects. *Magma*. 2006;19:55-61.
32. Schulz J, Siegert T, Bazin PL, et al. Prospective slice-by-slice motion correction reduces false positive activations in fMRI with task-correlated motion. *Neuroimage*. 2014;84:124-132.
33. Setsompop K, Gagoski BA, Polimeni JR, Witzel T, Wedeen VJ, Wald LL. Blipped-controlled aliasing in parallel imaging for simultaneous multislice echo planar imaging with reduced g-factor penalty. *Magn Reson Med*. 2012;67:1210-1224.
34. Faraji-Dana Z, Tam F, Chen JJ, Graham SJ. Interactions between head motion and coil sensitivity in accelerated fMRI. *J Neurosci Methods*. 2016;270:46-60.
35. Cauley SF, Polimeni JR, Bhat H, Wald LL, Setsompop K. Inter-slice leakage artifact reduction technique for simultaneous multislice acquisitions. *Magn Reson Med*. 2014;72:93-102.
36. Pruessmann KP, Weiger M, Scheidegger MB, Boesiger P. SENSE: sensitivity encoding for fast MRI. *Magn Reson Med*. 1999;42:952-962.
37. Qu P, Wang C, Shen GX. Discrepancy-based adaptive regularization for GRAPPA reconstruction. *J Magn Reson Imaging*. 2006;24:248-255.

38. Uecker M, Lai P, Murphy MJ, et al. ESPIRiT-an eigenvalue approach to autocalibrating parallel MRI: where SENSE meets GRAPPA. *Magn Reson Med.* 2014;71:990-1001.
39. Debbins JP, Felmlee JP, Riederer SJ. Phase alignment of multiple surface coil data for reduced bandwidth and reconstruction requirements. *Magn Reson Med.* 1997;38:1003-1011.
40. Ying L, Sheng J. Joint image reconstruction and sensitivity estimation in SENSE (JSSENSE). *Magn Reson Med.* 2007;57:1196-1202.
41. Huang L-K, Wang M-JJ. Image thresholding by minimizing the measures of fuzziness. *Pattern Recogn.* 1995;28:41-51.
42. Blaimer M, Breuer F, Mueller M, Heidemann RM, Griswold MA, Jakob PM. SMASH, SENSE, PILS, GRAPPA: how to choose the optimal method. *Top Magn Reson Imaging.* 2004;15:223-236.
43. White N, Roddey C, Shankaranarayanan A, et al. PROMO: real-time prospective motion correction in MRI using image-based tracking. *Magn Reson Med.* 2010;63:91-105.
44. Gallichan D, Marques JP, Gruetter R. Retrospective correction of involuntary microscopic head movement using highly accelerated fat image navigators (3D FatNavs) at 7T. *Magn Reson Med.* 2016;75:1030-1039.
45. Wallace TE, Afacan O, Waszak M, Kober T, Warfield SK. Head motion measurement and correction using FID navigators. *Magn Reson Med.* 2019;81:258-274.
46. Thesen S, Heid O, Mueller E, Schad LR. Prospective acquisition correction for head motion with image-based tracking for real-time fMRI. *Magn Reson Med.* 2000;44:457-465.
47. Steger TR, Jackson EF. Real-time motion detection of functional MRI data. *J Appl Clin Med Phys.* 2004;5:64-70.
48. Hennel F, Buehrer M, von Deuster C, Seuven A, Pruessmann KP. SENSE reconstruction for multiband EPI including slice-dependent N/2 ghost correction. *Magn Reson Med.* 2016;76:873-879.
49. Lyu M, Barth M, Xie VB, et al. Robust SENSE reconstruction of simultaneous multislice EPI with low-rank enhanced coil sensitivity calibration and slice-dependent 2D Nyquist ghost correction. *Magn Reson Med.* 2018;80:1376-1390.

How to cite this article: Li B, Li N, Wang Z, Balan R, Ernst T. Simultaneous multislice EPI prospective motion correction by real-time receiver phase correction and coil sensitivity map interpolation. *Magn Reson Med.* 2023;1-17. doi: 10.1002/mrm.29789